Large Eddy Simulation of Stenotic Flow for Wall Shear Stress Estimation - Validation and Application

ROLAND GÅRDHAGEN
Linköping University
Dept. of Management and Engineering
SE-581 83 Linköping
SWEDEN
roland.gardhagen@liu.se

JONAS LANTZ
Linköping University
Dept. of Management and Engineering
SE-581 83 Linköping
SWEDEN
jonas.lantz@liu.se

FREDRIC CARLSSON
FS Dynamics Sweden AB
Mölndalsvgen 24
SE-412 63 Gothenburg
SWEDEN
fredrik.carlsson@fsdynamics.se

MATTS KARLSSON
Linköping University
Dept. of Management and Engineering
SE-581 83 Linköping
SWEDEN
matts.karlsson@liu.se

Abstract: Turbulent flow in the cardiovascular system may increase the risk for severe arterial disease. This work addresses the feasibility of Large Eddy Simulation (LES) using a general purpose code as a tool for assessment of cardiovascular flow and investigates Wall Shear Stress (WSS) in steady as well as pulsating turbulent pipe flow. Poiseuille flow was specified at the inlet, and with a suitable ammount of perturbations at the inlet it was possible to predict experimental data. The extent of the recirculation zone was affected by the inlet disturbances, and magnitude as well as direction of the WSS vector varied significantly at the reattachment point. For the pulsating flow, WSS shows a complex pattern with different spatial and temporal variation along the pipe. The wall shear stress gradient was calculated on the entire post-stenotic surface and each component in the gradient was investigated. The off-diagonal components in the gradient are usually assumed to be small, but here they were found to be on the same order of magnitude as the diagonal terms. This work demonstrates the need for a scale resolving simulation technique to accurately model cardiovascular flows.

Key–Words: Turbulence, Large Eddy Simulation, Cardiovascular Flow, Wall Shear Stress

1 Introduction

Turbulence in the arterial blood flow may increase the risk for hemolysis [1] as well as platelet activation and thrombus formation [2, 3]. It is also suggested that turbulence may be involved in the pathogenesis of atherosclerosis [4, 5, 6]. The peak Reynolds number (Re) in the aorta is about 10 000 under normal resting conditions [4], thus, although pulsating, turbulence in the arterial system is not unlikely.

The interior surface of a blood vessel is covered with a single layer of cells, the endothelium, and apart from blood pressure the cells are subjected to a shear force, the Wall Shear Stress (WSS) from the blood, which can trigger cell alignment with flow direction [7, 8, 9, 10, 11]. Vascular WSS has also been correlated to cardiovascular disease, and considerable research has been done in this field. Close to arterial bifurcations and constrictions, flow characteristics such as separation, recirculation and reattachment alters the WSS signal, which can have aggravating effects on the endothelium [12, 13]. Also, the type of flow is important to consider when evaluating WSS; Davies *et al.* [11] performed experiments where they subjected cell monolayers to both laminar and turbulent flow, and found that endothelial cell turnover *in vitro* was considerably more sensitive to low shear stress in turbulent flow, than to high shear stress in laminar flow. The WSS signal affecting the cells in turbulent flow is fluctuating both in magnitude and direc-

tion, while in a laminar flow the signal is steady.

Several researchers [14, 15, 16, 17, 18] have proposed that the rate of change of WSS with respect to either time or position plays an important role in the injury of the endothelial cell layer. These wall shear stress *gradients* (WSSG), can injure the cells by causing e.g. high cell turnover, leaky cell junctions, enhanced permeability, or even cell-cell bond rupture [19].

Experimental *in vitro* studies of turbulent flows have been conducted in straight circular pipes with constrictions, representing idealized models of stenosed vessels. During the 1980's Giddens and co-workers [20, 21, 22, 23] used Laser Doppler Velocimetry (LDV) to study flows in axi-symmetric pipes with a cosine shaped stenosis of either a 25%, 50%, or 75% reduction of the cross sectional area. Reynolds numbers (Re) from 500 to 15000 were considered in steady flows and Reynolds numbers from 200 to 1000 in pulsating flows were investigated. The axial velocity component was measured, and mean as well as fluctuating components were determined. Post-stenotic turbulence was found for Reynolds numbers of 1000 or higher when the stenosis was 75 % in steady flow. For $Re = 250$ and $Re = 500$ the flow remained laminar, although periodic shear layer oscillations were detected in the latter case. The effect of pulsatility made the distal flow more disturbed than steady flow at the same mean Reynolds number.

Turbulent flows are inherently unsteady and characterized by three dimensional eddies. These range in size from the largest eddies, governed by geometrical and large scale flow features, to the smallest scales (known as the Kolmogorov scales) determined by the viscous dissipation. Davies *et al.* [11] calculated the Kolmogorov scale to be within a factor of 5 of an individual endothelial cell in their experiment, implying that significant shear stress gradients are present over distances comparable to cellular dimensions. Thus, reasonable modeling of the interaction between turbulent WSS and endothelial cells requires appropriate treatment of the smallest turbulent scales. Reynolds Averaged Navier-Stokes (RANS) models are relatively cheap to run but do not resolve any turbulent motion. No RANS model has yet succeeded to match velocity or turbulence quantities from measurements or Direct Numerical Simulation (DNS) predictions for this kind of pipe flow, and consequently, will not predict the turbulent WSS or WSSG either. DNS of the full Navier-Stokes equations is the most accurate computational method available for simulation of turbulent flows. In contrast to RANS modeling, a DNS resolves all of the turbulent motion in the flow. However, a DNS quickly becomes enormously costly in terms of computational resources when the Reynolds number is increased. The geometrical complexity of the model is also severely restricted due to the numerical methods used in DNS.

Large Eddy Simulation (LES) is a computational method that combines the advantages of RANS models and DNS. The large, energy carrying turbulent eddies are resolved in time and space, while the small eddies are modeled. Although the computational cost is considerably higher for LES compared to RANS, the cost is much less in comparison to DNS. Still, most of the flow dynamics of interest is resolved in LES, and it usually demonstrates a superior performance compared to RANS. Furthermore, transition to turbulence can be resolved with LES, and complex geometries are not a general limitation. In addition Antiga and Steinman [24] discussed the need of scale resolving techniques for appropriate modeling of the deformation of blood constituents.

Several studies in which turbulent pipe flow or channel flow is simulated have been presented. The standard and transitional $k - \omega$ models were compared to LDV measurements [21, 22] for both pulsating and non-pulsating flows using a fully three-dimensional model of a stenosed pipe with a 75% stenosis [25]. The effects of imposing small disturbances at the inlet were investigated. Velocity profiles partly agreed with measurements for $Re = 500$ and $Re = 1000$, and center line turbulence intensity agreed qualitatively if low disturbances were imposed at the inlet, although the onset of turbulence occurred later compared to the findings in the experiments.

An initial study of the possibilities for LES to be used for turbulent cardiovascular flows was was presented in [26]. The geometry was a planar channel with a semicircular half sided stenosis

using a combined finite difference spectral solver. Post-stenotic turbulence was observed with all its complex attributes, and the potential of LES for accurate prediction of cardiovascular flows was demonstrated.

Mittal *et al.* [27] applied LES and DNS to pulsatile flow of peak Reynolds numbers between 750 and 2000 in a planar channel with a one sided stenosis. Their findings demonstrate post-stenotic transition to turbulence for Reynolds number greater than 1000. Transition takes place where the separated shear layer reattaches to the wall, and is associated with high shear stress oscillation. For Re $\leq$ 1000, the absence of an inertial shear layer indicates no full transition to turbulence, which is in agreement with experimental observations [21].

DNS using a high-order spectral element method was applied to model the flow in a stenosed carotid bifurcation [28]. For mean and peak Reynolds numbers of 266 and 911, respectively, the results revealed post-stenotic transitional behavior during systole and laminar flow during diastole. High WSS was observed in the stenosis, and large WSSG appeared as a result of flow separation.

DNS has also been used to study transitional flow in circular pipes with both symmetric and eccentric stenoses [29, 30]. Steady as well as pulsatile flows with Reynolds numbers ranging from 200 to 1000 were investigated. A fully developed, disturbance free velocity profile was imposed at the inlet, and a geometrical eccentricity was introduced at the stenosis to trigger post-stenotic turbulence. The steady flow transitioned to turbulence about 5 diameters downstream, with the velocity spectra taking a broadband nature, with the usual -5/3 slope. The sensitivity of stenosis degree was investigated, using three geometries: 70, 73 and 75 % area reduction. It was found that the velocity profiles matched experimental data perfectly immediately downstream for the 73 % case. Further downstream the profiles diverged and the simulated flow reattached much further downstream compared to the experimental data. The pulsatile flow was simulated to investigate the periodic transition and relaminarization of post-stenotic flow. The results indicated that early and mid-acceleration phases were relatively stable with no turbulent activity after the stenosis. However, at the end of the acceleration phase, vortex breakup was found and a turbulent location was formed in the poststenotic region, with breakdown of streamwise vortices at peak flow. During the deceleration phase the flow lost its momentum and began to relaminarize. The breakdown at peak flow resulted in high WSS levels in the turbulent region, with large axial and circumferential fluctuations. Same authors also presented one of the more thorough RANS studies in which the RNG $k-\epsilon$ model, the realizable $k-\epsilon$ model, a $k-\omega$ model, and a Reynolds Stress Model (RSM) were used in the eccentric stenosis for a flow with a Reynolds number of 1000 [31]. The results were compared to the DNS data, but a poor agreement was observed for all models. It is noticeable that the more sophisticated RSM did not perform better than the two-equation models.

A few studies where LES is applied for turbulent pipe flow have been presented. Mittal *et al.* [26, 27] conducted the most thorough; both LES and DNS were evaluated. Their work concerned pulsatile flow in a rectangular pipe with a one-sided semi-circular constriction (50% area reduction); the authors comment that the geometry does not account for the circular cross section of a typical artery, and call for further studies using more realistic geometries.

Varghese *et al.* [31] also performed LES of the flow in a circular pipe with an eccentric stenosis, however time averaged quantities were not obtained. They concluded that LES might offer a promising route towards predicting transitional stenotic flows, but added that the computational cost is greater compared to traditional turbulence models.

The studies mentioned above have shown the complexity of cardiovascular flows as well as the potential of LES as a simulation tool. Most of them have used high-order research codes. In this work the aim is first to validate a general-purpose code, i.e. a code not developed for a particular application, against available experimental data. An investigation of the sensitivity to outer disturbances is conducted, in order to evaluate whether a certain amount of inlet disturbances can be imposed to control transition and hence reproduce

Figure 1: The circular pipe used for the computations.

experimental data. Secondly, LES, as a scale resolving technique, is applied for estimation of WSS and WSSG patterns in steady and pulsatile turbulent flows.

2 Method

The geometry consisted of a circular pipe with a cosine shaped stenosis previously described by [20], Fig. 1. A 75% reduction of the cross-sectional area was prescribed at the stenosis throat. Upstream of the stenosis the length of the pipe was 4 diameters, D, and the downstream length was 20 D, Fig. 1. These distances were based on a boundary position study conducted by Ryval *et al.* [25].

2.1 Large Eddy Simulation

The governing equations for LES are obtained by spatial filtering of the time-dependent Navier-Stokes equations. Filtering is conducted using a filter width, $\bar{\Delta}$, corresponding to the grid size, and a filtered variable $\bar{\phi}$ is obtained as

$$\bar{\phi} = \frac{1}{V}\int_V \phi(\mathbf{x})d\mathbf{x}. \tag{1}$$

Scales that are smaller than the filter width are referred to as sub-grid scales (SGS). For a fluid with density ρ, velocity components u_i, pressure p, and kinematic viscosity ν, the filtered continuity and momentum equations are:

$$\frac{\partial}{\partial x_i}\left(\bar{u}_i\right) = 0, \tag{2}$$

$$\frac{\partial \bar{u}_i}{\partial t} + \frac{\partial}{\partial x_j}\left(\bar{u}_i\bar{u}_j\right) = -\frac{1}{\rho}\frac{\partial \bar{p}}{\partial x_i} + \frac{\partial}{\partial x_j}\left(\nu\frac{\partial \bar{u}_i}{\partial x_j}\right) - \frac{\partial \tau_{ij}}{\partial x_j}. \tag{3}$$

The sub-grid stress tensor τ_{ij} is defined by

$$\tau_{ij} = \overline{u_i u_j} - \bar{u}_i\bar{u}_j. \tag{4}$$

The deviatoric part of the sub-grid stresses were modeled using the dynamic Smagorinsky-Lilly model [32, 33, 34], giving

$$\tau_{ij} - \frac{1}{3}\tau_{kk}\delta_{ij} = -2\nu_t\bar{S}_{ij}, \tag{5}$$

where ν_t is the SGS turbulent viscosity, τ_{kk} is the isotropic part of the SGS stress tensor (which for incompressible flow is negligibly small), and $\bar{S}_{ij}$ is the rate-of-strain tensor of the resolved turbulence defined by

$$\bar{S}_{ij} = \frac{1}{2}\left(\frac{\partial \bar{u}_i}{\partial x_j} + \frac{\partial \bar{u}_j}{\partial x_i}\right). \tag{6}$$

The turbulent viscosity is now obtained as

$$\nu_t = L_s^2|\bar{S}|, \tag{7}$$

where L_s is the mixing length,

$$L_s = min(\kappa d, C_s\Delta), \tag{8}$$

determined by the von Kármán constant κ, the distance to the closest wall d, the cubic root of the cell volume Δ, and the Smagorinsky constant C_s. The latter is computed dynamically using information from the resolved scales.

The simulations were carried out using ANSYS Fluent 6.3 (ANSYS, Inc., Canonsburg, PA, USA), which employs a cell-centered finite-volume method. For all simulations the fluid was assumed to be incompressible and Newtonian. A segregated solver with the fractional-step solution algorithm was used, and time control was obtained using a non-iterative time advancement scheme. The time step was set to get a Courant number less than 1, and the flow was initialized with the average velocity at the inlet. All simulations were run on the Linux clusters Neolith and Kappa at National Supercomputer Centre (NSC), Linköping University, Sweden.

Diffusive and convective fluxes were discretized using second-order central differencing, and the pressure at a cell face was computed using a discrete continuity balance for a staggered control volume. A fully implicit second order scheme was used for the temporal discretization.

Poiseuille flow was specified at the inlet, and perturbations representing outer disturbances were superimposed onto the laminar velocity profile. For the unsteady case the temporal pulse profile varied according to the mass flow rate obtained from Magnetic Resonance Imaging from

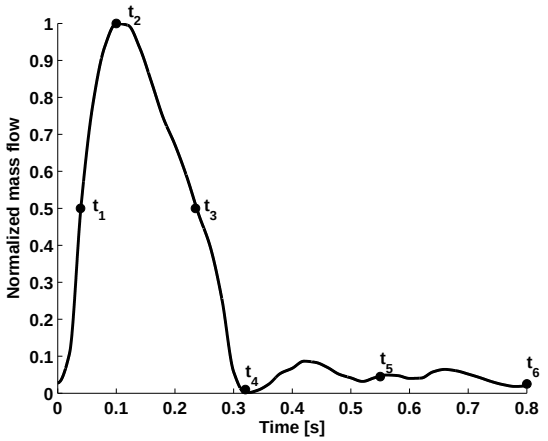

Figure 2: Normalized mass flow rate for the pulsatile flow. The time points indicated are used for WSS assessment.

a young healthy male under resting conditions, Fig. 2. The peak Reynolds number was 2644. At the outlet a static pressure was specified, while all other properties were extrapolated from the interior solution. No-slip was prescribed at the pipe surface and the walls were rigid.

The inlet perturbations were generated using a variant of the vortex method [35, 36]. It produces a spatially correlated disturbance field depending on a specified intensity I_{in}, the mesh size, and the time step size. Unphysical numerical oscillations commonly obtained for completely random disturbances that may deteriorate the solution are thus avoided. Three distinct cases of inlet intensities were considered: none (NP), small (SP), and large (LP) perturbations corresponding to $I_{in} = \{0, 1\%, 10\%\}$. As a special case $I_{in} = \{15\%\}$ was also tested and will be denoted very large perturbations (VLP). As these are purely artificial and superimposed onto a laminar profile, their magnitude will adjust downstream from the inlet. Before entering the stenosis the fluctuations are of the same size as the experimental observations, which was the desired.

The simulations were performed on a fully structured mesh containing 6 million cells (MC), with reduced cell size in the stenotic and poststenotic regions. In the vicinity of the pipe wall the cell size was also gradually reduced. The non-dimensional wall distance y^+ was less than 0.2 in the fully turbulent region for $Re = 2000$. ANSYS Gambit 2.4 (ANSYS, Inc., Canonsburg, PA, USA) was used for the meshing. A grid independence test was performed for $Re = 2000$ using large perturbations at the inlet. Root mean square values of the axial velocity fluctuations for the 6 MC mesh were compared to results obtained with a 12 MC mesh, Fig. 3. Z is a non-dimensional coordinate indicating the axial position downstream of the stenosis in unoccluded diameters, i.e. Z = 0 corresponds to the throat of the stenosis. Regions of acceleration and deceleration coincided, and the difference was less than 4%. Same behavior was seen when comparing WSS, and hence grid convergence was considered to be achieved. No effort was made to minimize the number of cells in the mesh.

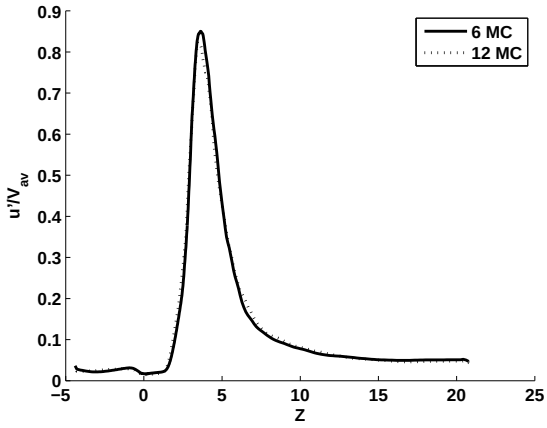

Figure 3: Results from the 6 MC-mesh are compared to results from a 12 MC-mesh through the entire pipe confirming grid independence ($Re = 2000$, LP). Z is the axial coordinate non-dimensionalized by the unoccluded diameter. The difference at every axial location is less than 4%.

2.2 Wall Shear Stress Components

Since WSS only exists parallel to a surface, it can be described as a two-component vector $\boldsymbol{\tau_w} = (\tau_m, \tau_n)$, where τ_m denotes the WSS component in the mean flow direction and τ_n the WSS component tangential to the surface and normal to τ_m. From the simulations the WSS vector was given in Cartesian coordinates as $\boldsymbol{\tau_w} = (\tau_{w,x}, \tau_{w,y}, \tau_{w,z})$, which therefore had to be mapped into m, n-components. The τ_m component equals the $\tau_{w,x}$ component in the Carte-

sian coordinate system since the mean flow is in the (axial) x direction, while the τ_n component points in the circumferential direction and was calculated as the magnitude of the $\tau_{w,y}$ and $\tau_{w,z}$ components:

$$\tau_m = \tau_{w,x} \tag{9}$$

$$\tau_n = \sqrt{\tau_{w,y}^2 + \tau_{w,z}^2} \tag{10}$$

The WSS components were evaluated on each of the mesh points on the entire post-stenotic surface, yielding some 50 000 data points per time step. To get statistical convergence on the gradient calculations, 12 000 time steps were used, corresponding to a flow time of 0.6 s (steady state). WSS was also monitored in one point at every diameter downstream of the stenosis in order to evaluate the temporal angular variation of the shear stress vector.

2.3 Wall Shear Stress Gradient

When the axial and circumferential WSS components are known, the gradient $\nabla \boldsymbol{\tau_w}$ (WSSG) can be computed by taking the spatial derivatives of $\boldsymbol{\tau_w}$, as:

$$\nabla \boldsymbol{\tau_w} = \begin{bmatrix} \frac{\partial \tau_m}{\partial m} & \frac{\partial \tau_m}{\partial n} \\ \frac{\partial \tau_n}{\partial m} & \frac{\partial \tau_n}{\partial n} \end{bmatrix} \tag{11}$$

The gradient was calculated using second-order finite differences which accounted for non-uniformity in spatial step size in the axial direction. The WSSG is an asymmetric second-order tensor with four components, and it has been hypothesized that the diagonal components $\frac{\partial \tau_m}{\partial m}$ and $\frac{\partial \tau_n}{\partial n}$ are responsible for intracellular tension and that the off-diagonal components $\frac{\partial \tau_m}{\partial n}$ and $\frac{\partial \tau_n}{\partial m}$ are responsible for intracellular shearing [19, 37, 38, 39]. In a uniform flow field the WSSG would be equal to zero, so wherever WSSG is non-zero the flow environment is nonuniform.

A common parameter using WSSG components for correlation with vascular diseases is $|\mathrm{WSSG}_S|$, [40, 41, 42, 43], defined as:

$$|\mathrm{WSSG}_S| = \sqrt{\left(\frac{\partial \tau_m}{\partial m}\right)^2 + \left(\frac{\partial \tau_n}{\partial n}\right)^2} \tag{12}$$

In Eqn. 12 the off-diagonal components in $\nabla \boldsymbol{\tau_w}$ are neglected and only the intracellular tension generating components are considered. This is because it is hypothesized that those two components are the ones contributing most strongly to cell turnover, gap widening and bond rupture between endothelial cells [19, 38]. However, even though large time averaged $|\mathrm{WSSG}_S|$ values have been correlated with the onset of atherosclerosis [41, 44], and sites of increased neointimal hyperplasia [41, 45, 46, 47], it is not certain that the off-diagonal terms can be neglected. As will be shown in this paper, their magnitude can be of the same size or sometimes even larger than the diagonal terms, and may therefore also contribute to cell deformation.

3 Results and Discussion

Pulsating and non-pulsating flows in an axisymmetric stenosed pipe have been investigated in order to assess the feasibility of LES using a general purpose code for simulation of flows in subject specific vessel models, and to investigate how turbulence affects WSS. Non-pulsating flows of $Re = 500$, $Re = 1000$, and $Re = 2000$ were simulated since measurements and/or DNS predictions were available, and the solver could be validated. The pulsating flow was based on a physiological pulse profile with a peak Reynolds number of 2644.

All presented velocities are normalized by the average inlet velocity, V_{av}. Instantaneous axial velocity was monitored continuously in a number of points along the center line for the non-pulsating cases, and sampling of statistical data was started when the initial transients had disappeared. Convergence was considered achieved when the time averaged values had leveled out.

3.1 Solver Validation

To ensure that the basic solver settings and numerics are appropriate a simulation with $Re = 500$ LES predictions were compared to DNS [29] predictions and experimental values [21].

Fig. 4 shows velocity profiles at various locations downstream of the stenosis. R is the local

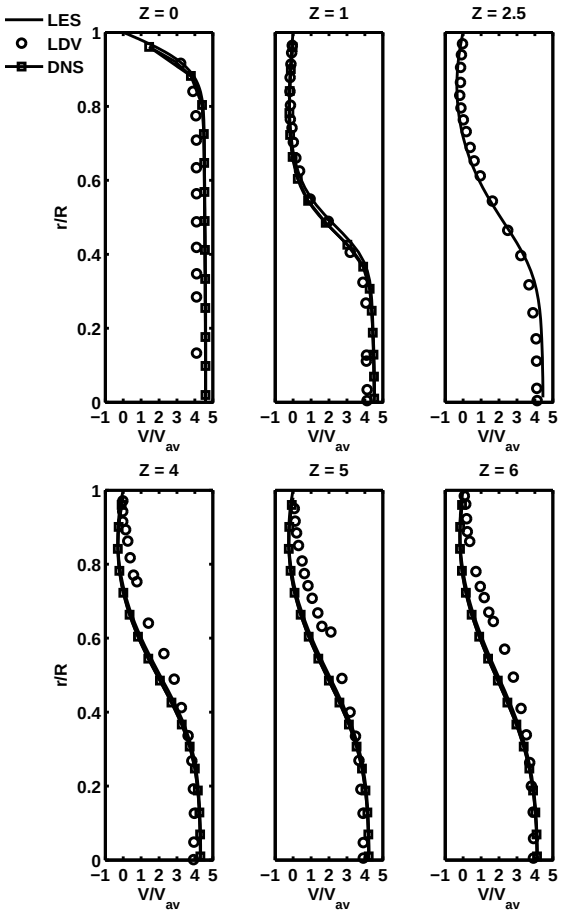

Figure 4: Velocity profiles for $Re = 500$. LES predictions are compared to LDV measurements [21] and DNS predictions [29]. R is the local pipe radius and r the radial coordinate.

pipe radius and r the radial coordinate. Four velocity profiles were extracted at each cross section and used to compute an average profile. Perfect agreement was found between LES without inlet disturbances and DNS; the latter were run without any imposed perturbations. Hence, it was assumed that the basic settings were appropriate for the present problem. No turbulence was observed; and disturbances at the inlet merely resulted in oscillations in the shear layer, which was also found in the experiments [21] and discussed by [48]. The ratio of the turbulent viscosity to the molecular viscosity was essentially zero, also indicating that all the motion was resolved.

Inlet perturbations of various degrees were applied in order to represent outer disturbances of any kind possibly affecting *in vitro* as well as *in vivo* flow. These were generated using a variant of the vortex method, by which the specified intensity determines the magnitude of the perturbations on the mean velocity components. As the perturbations are artificial they will adjust to fit the flow during the entrance of the pipe, see Fig.5 showing normalized fluctuations of the axial velocity component. The imposed perturbations result in fluctuations of about 3% or less of the mean axial velocity prior to the stenosis. Further reduction of the fluctuations is seen due to the acceleration before the stenosis (located between Z = -1 and Z = 1) although the levels are still 1 % to 1.5%. Thus at the stenosis the fluctuations are compareable with the measurements [22] and they prevail through the stenosis.

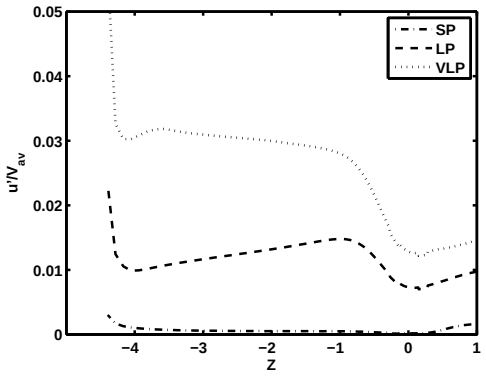

(a)

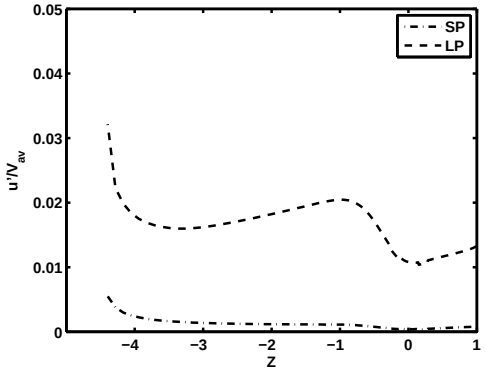

(b)

Figure 5: Fluctuation of the axial velocity component in the inlet section for $Re = 1000$ (a) and 2000 (b). The disturbances decreased rapidly from the specified inlet values adjusting to physical levels for the present flow. In addition, they also affect the flow in the post stenotic region. SP: small perturbations, LP: large perturbations, and VLP: very large perturbations.

The lowest Reynolds number for which tur-

bulence was detected in the experiments was 1000 [21]; the DNS on the other hand did not indicate any transition for this Reynolds number as long as the flow was undisturbed.

Without inlet disturbances, LES predictions showed a large time scale intermittent behavior where the transitional region moved back and forth between the outlet and Z $\approx$ 3 in cycles altered by completely laminar flow. Since this behavior was not seen in the DNS, it can probably be derived to differeces in the numerics between the LES and the DNS. For simplicity, (regarding the undisturbed case only) statistics was only collected during the laminar periods. Time averaged velocity profiles and centerline fluctuations are shown in Fig. 6 and Fig. 7, respectively. DNS predictions, which were obtained without disturbances and did not show any post-stenotic transition [29], are replicated perfectly by the laminar, undisturbed flow, whereas the experimental observations are approached as the disturbances increase. Addition of a perturbation always resulted in post-stenotic turbulence; the larger the disturbance the shorter the distance between the stenosis and the reattachment point. For SP transition occurred after Z = 6, which explains the good agreement for this case with the DNS in Fig. 6. A similar behavior is seen for the velocity fluctuations. At the throat the highly disturbed flow is closest to the measurements, but does still not reach these, hence the VLP case corresponding to $I_{in} = 15\%$ was conducted. Apparently this was somewhat too large and additional studies revealed that the optimal inlet disturbance in this case was close to 13 % (not shown here). The fluctuations decreases quickly towards the exit, but remains above 5% throughout the pipe indicating that no relaminarization takes place.

As the agreement with DNS predictions is satisfactory and the transition can be controlled by suitable amounts of perturbation at the inlet the solver settings and numerics was considered adequate for the present flow, and the study was continued to simulate steady flow of Re = 2000, for which there are measurements, but still no successful numerical replication of these. RANS models have failed, whereas no attempts with scale resolving techniques to our knowledge have yet been published. In addition, this case al-

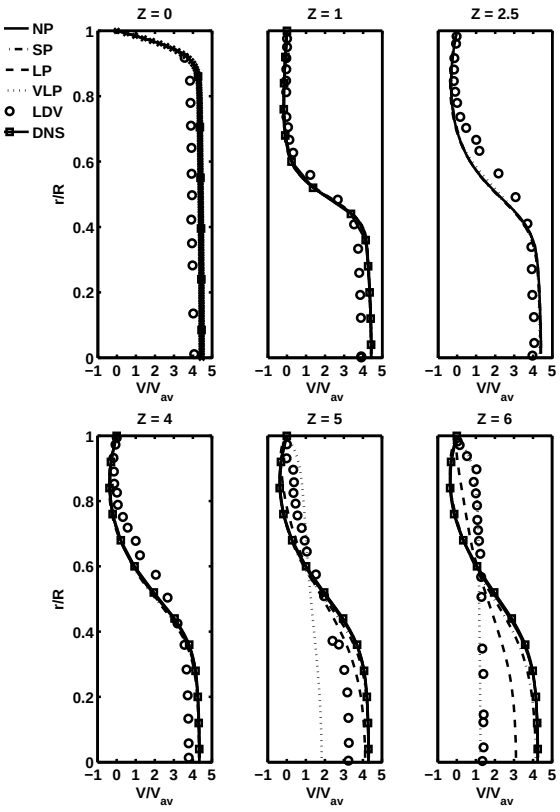

Figure 6: Velocity profiles for $Re = 1000$. LES predictions are compared to LDV measurements [21] and DNS predictions [29]. R is the local pipe radius and r the radial coordinate. For the DNS data, the boxes only distinguish the lines, they do not indicate discrete values. NP: no perturbations, SP: small perturbations, LP: large perturbations, VLP: very large perturbations.

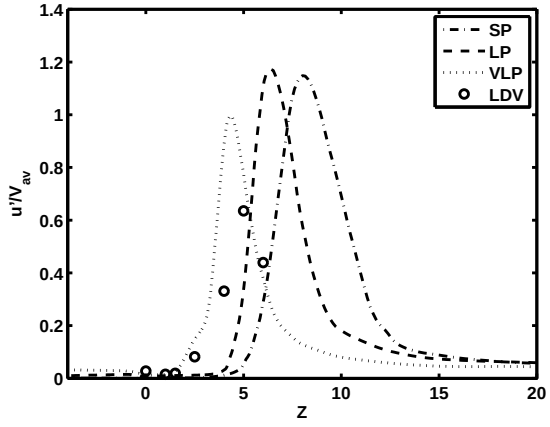

Figure 7: Fluctuation of the axial velocity component for $Re = 1000$ along the center line. Experimental data from [22].

lows for a characterization of WSS in turbulent flow using a general purpose code. LES has previously been applied to pulsating flows with a peak Reynolds number less than 2000 in a planar channel [26, 27]; but flows in circular pipes of $Re = 2000$ have only been studied using statistical turbulence models, and as pointed out these models are yet to be validated against LES or DNS [29].

Time averaged velocity profiles at various axial locations are show in Fig. 6. Post-stenotic turbulence was always observed, even for the case without inlet perturbations, and a blunt turbulent velocity profile was always developed before Z = 6 independent of the disturbances at the inlet. The location of the transition point could be controlled by the disturbances, and in this case, the medium sized perturbation created a flow field in close agreement with the experiments [21], where a recirculation zone extending to Z $\approx$ 2.8 was observed. The LP LES predicted a corresponding reattachment at Z $\approx$ 3.3. Without disturbances the reattachment point was located at Z $\approx$ 4.4.

Instantaneous velocity profiles for LES with large perturbations, Fig. 9, show a smooth profile at the stenosis throat, whereas the profile at Z = 2 suggests a more complex flow field where the vortical structures from the broken shear layer marks the profile. Relatively quickly, however the size of the structures is decreased and the profiles develop towards the known blunt shape further downstream. This is further supported by Fig. 10 showing instantaneous vorticity magnitude for the LP case. A shear layers develops from the stenosis and rolls up into smaller vortices. There is no distinct development of a shear layer along the pipe wall which was found in [27]. However, isolated spots of high vorticity after the shear layer roll up suggest oscillatory shearing at the pipe surface, which in turn can affect the function of endothelial cells in this region.

Turbulent fluctuations along the center line for the axial velocity component are shown in Fig. 11. For no and small perturbations only minor differences between the curves could be distinguished, and the transition as well as recovery of the flow occurred further downstream

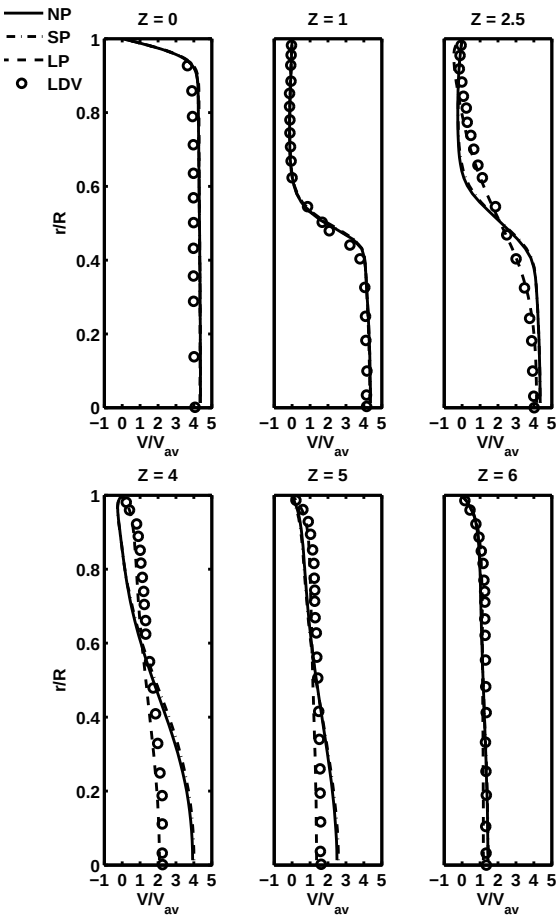

Figure 8: Velocity profiles for $Re = 2000$. The LES predictions are compared to LDV measurements [21]. R is the local pipe radius and r the radial coordinate.

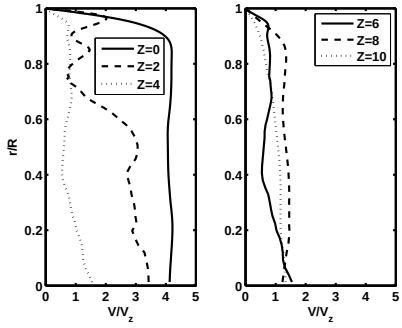

(a)

Figure 9: Instantaneous velocity profiles for $Re = 2000$, LP. R is the local pipe radius and r the radial coordinate.

(a)

Figure 10: Instantaneous vorticity for $Re = 2000$, LP, in a plane through the stenosis. White is counter clockwise and black is clockwise.

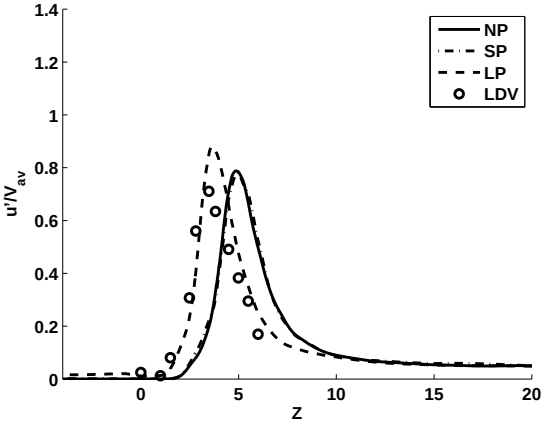

Figure 11: Fluctuation of the axial velocity component for $Re = 2000$ along the center line. Experimental data from [22].

compared to the experiments. The large perturbation, however, matched the experimental turbulence intensities along the pipe. The width of the turbulent region was basically unaffected by the amount of disturbances applied at the inlet. All simulated flows also showed remaining turbulence all the way to the exit, thus no complete relaminarization occurred. The effect of the varied inlet disturbance is, as indicated in Figs. 8 and 11, mainly a change in the location of the reattachment point.

Whereas RANS models have failed to reproduce the experimental data also for this Reynolds number [49, 50], LES seems to be capable of capturing the flow behavior in the stenosed pipe. A problem reported for RANS models [25] was that a high inlet disturbance provoked onset of turbulence in or even before the stenosis throat. According to Fig. 11 this did not occur with LES, instead the onset of turbulence always accompanied the jet break-down in the post-stenotic region.

Being a scale resolving technique LES should resolve the larger turbulent structures of the flow whereas the smaller ones are modeled. In Fig. 12 the structures of the turbulence are illustrated by the normalized Q-criterion [35]. It can be seen that smaller structures reside in the post stenotic area where the jet breaks down, whereas larger and longer structures form as the

Figure 12: Turbulent structures in the flow. $Re = 2000$, LP, visualized by the normalized Q criterion.

3.2 Wall Shear Stress

As shown in the previous section the velocity field is characterized by pronounced turbulent fluctuations. Thus, parameters derived from the velocity field should be expected to fluctuate accordingly. Under the assumption of a Newtonian fluid, WSS is directly proportional to the velocity gradients, and oscillatory WSS has been correlated with the risk to develop atherosclerotic lesions. A thorough investigation of the WSS in a turbulent flow is therefore of great importance. Rose plots in Figs. 13 and 14 show the directional distribution of the WSS vector at various post-stenotic locations (points) sampled during 200 000 time steps, or 10 seconds flow time for NP and LP, respectively. Zero degrees correspond to a WSS completely aligned with the pipe axis and directed downstream. Each sector of a rose plot represents an angular interval of 7.2° of the WSS vector.

Both figures indicate retrograde WSS in the immediate post-stenotic region, corresponding to the recirculation zone, no dominant direction at reattachment, and WSS aligning with the main flow direction further downstream. Consequently, WSS at the reattachment point is very oscillatory.

In the present study the walls are rigid, however in a study by Lantz *et al.* the WSS and wall motion in a subject specific human aorta were computed using fluid-structure interaction (FSI) and the results were compared with a rigid wall assumption [51]. It was found that the influence of wall deformation on the time-averaged WSS was low, while instantaneous WSS values differed between the FSI and rigid models. Therefore, when regarding time-averaged WSS values the rigid wall assumption is valid.

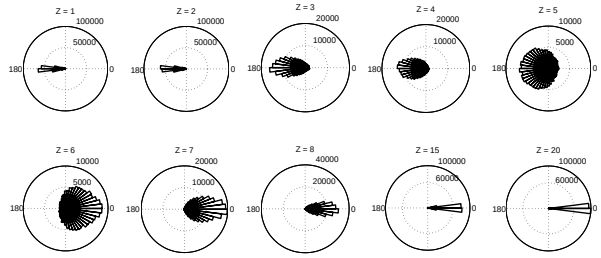

Figure 13: Directional distribution of the WSS vector for NP, calculated from 10 s flow time at various locations along the pipe for undisturbed flow at the inlet. WSS directed in the main flow direction (along the axis of the pipe) corresponds to 0°.

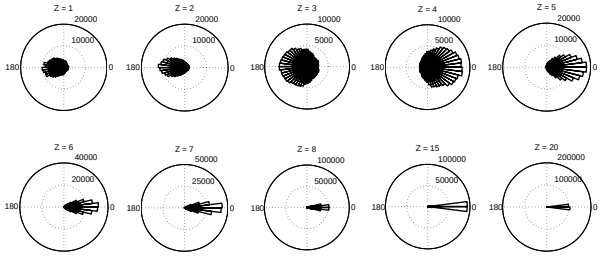

Figure 14: Directional distribution of the WSS vector for LP, calculated from 10 s flow time at various locations along the pipe for undisturbed flow at the inlet. WSS directed in the main flow direction (along the axis of the pipe) corresponds to 0°.

As the WSS vector does not point in a certain direction inside the reattachment zone, WSSG was computed to further analyze the WSS behavior. When regarding the WSSG, it has previously been assumed that the diagonal terms are the ones most responsible for pathological processes. This has been manifested by the $|\mathrm{WSSG}_S|$-parameter, Eq. 12, which uses the diagonal components in the gradient. However, to get a better understanding of the impact of the WSSG, all four components of the gradient are here considered. The magnitude of each of the components is first averaged at each cross-section and then averaged over time, and plotted against the axial coordinate Z, Fig. 15. The largest magnitude for all components coincide with the (average) reattachment point which is located at $Z \approx 4.4$ for NP and $Z \approx 3.3$ for LP.

The $\frac{\partial \tau_n}{\partial n}$ component is more than twice as large as the three other components at reattachment in the undisturbed case, while it is equal in magnitude compared to $\frac{\partial \tau_m}{\partial m}$ in the disturbed case. In both cases the magnitudes are of the same order, about 10^9 Pa/m, inside the recirculation zone. It is noticeable that $\frac{\partial \tau_m}{\partial m}$ has the fastest decay rate in both cases, and becomes the least significant component after the recirculation zone.

In the recirculation zone the off-diagonal terms are equal or lower in magnitude compared to the diagonal terms. However, the $\frac{\partial \tau_m}{\partial n}$ component has the slowest decay rate, and it is even the largest component in the gradient after the recirculation region. Before and after reattachment the magnitudes are equal (except $\frac{\partial \tau_n}{\partial n}$), it is only the peak values that differ, which in addition are strongly dependent of the inlet conditions. When calculating the $|\mathrm{WSSG}_S|$-variable the off-diagonal terms are often neglected as it has been hypothesized that they are much smaller, and thus, do not contribute to pathological processes. However, this work shows that all components in the WSSG gradient can be on the same order of magnitude, making the assumption of neglecting the off-diagonal components questionable.

3.3 Unsteady Flow

Pulsating flow based on a physiologically relevant pulse profile, see Fig. 2, was investigated in order to assess the WSS pattern during a pulse.

Instantaneous plots of vorticity magnitude along the pipe are shown in Fig. 16. Similarly to [27] at maximum acceleration, a shear layer

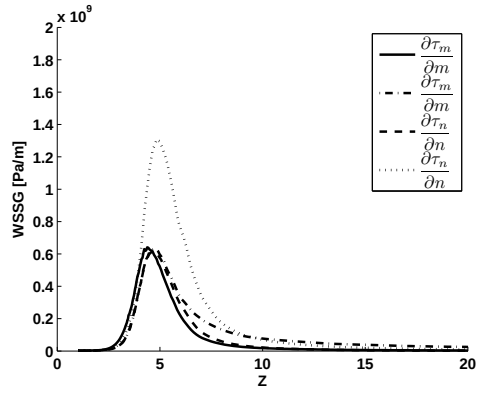

(a)

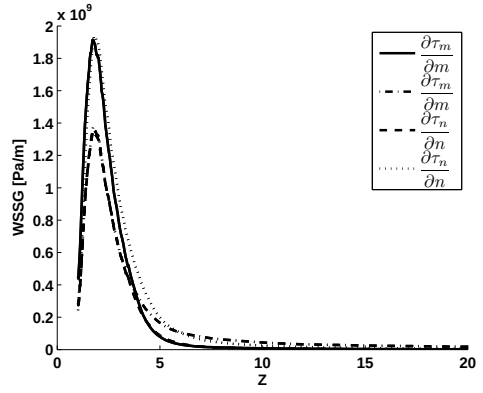

(b)

Figure 15: The WSSG magnitude of each of the four components in the gradient. (a) NP, (b) LP.

develops from the stenosis throat and separates. In the circular pipe the vortex is also circular at this instant and interacts with another shear layer developing along the pipe surface. At peak systole, i.e. when the inflow is at its maximum, the flow is characterized by several vortical structures, although the larger structures seen in the channel flow do not appear. At maximum deceleration the shear layers exist further downstream, as was also the case for the channel flow.

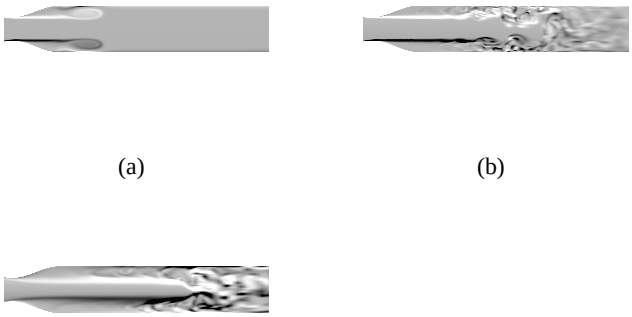

(a) (b)

(c)

Figure 16: Vorticity magnitude in the stenotic area at (a) maximum acceleration, (b) maximum inflow (peak systole), and (c) maximum deceleration. The whiter the higher magnitude.

Thy angular distribution of the WSS vector was investigated during a pulse, and the results are shown in Fig. 17 at various positions along the pipe, and during different parts of the pulse. Before maximum acceleration, i.e. during Δt_{12}, Fig. 2 index 12 refers to the time between point 1 and two, the WSS is directed forward along the entire pipe, without any significant directional changes. Around peak systole (during Δt_{23}), on the other hand, the WSS vector shows a oscillative behavior in the immediate post stenotic region, where the endothelial cells would be subjected to loads in all possible directions. Further downstream the onset of oscillatory WSS is somewhat delayed, and due to viscous damping not as pronounced as for Z $\leq$ 4. The late deceleration phase (Δt_{34}) is characterized by retrograde WSS for Z $\leq$ 4, whereas oscillations still prevail further downstream. During diastole (Δt_{45} and

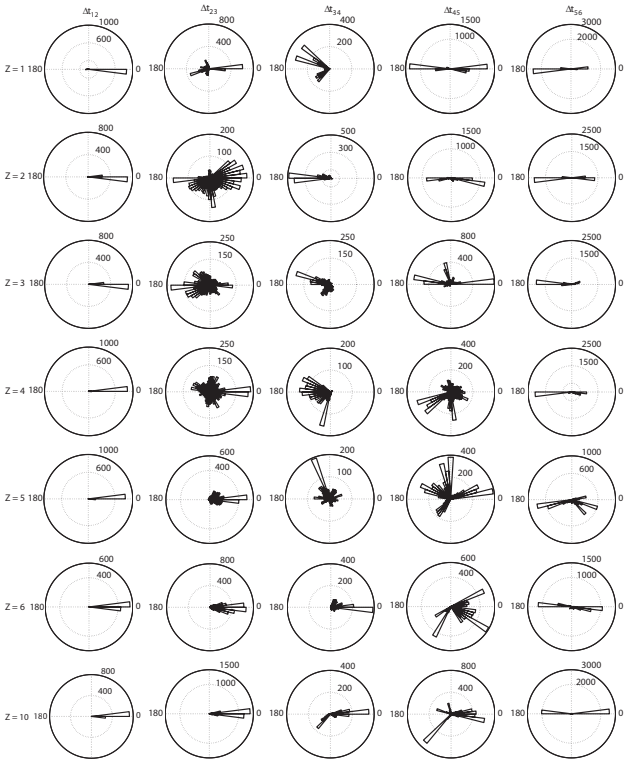

Figure 17: Directional distribution of the WSS vector for unsteady flow calculated during one pulse at various locations along the pipe. WSS directed in the main flow direction (along the axis of the pipe) corresponds to 0°. Each column corresponds to the time between to instants in Fig. 2

Δt_{56}) the oscillations progress towards the outlet, and during end diastole the flow mainly shift between forward and backward, with the former dominating in the first half of the pipe.

4 Concluding Remarks

In this work the feasibility of LES, using a general purpose code, for cardiovascular applications has been demonstrated. It was shown to manage to predict experimental data of turbulent flows in a stenosed pipe for Reynolds numbers up to 2000. Characteristic features for turbulent flows demonstrated by high order solvers for similar flows are also found in this study.

For steady flow the WSS pattern changes along the pipe, from being directed backwards in the recirculation zone to a clear forward direction further downstream. At the reattachment point, there is no dominant direction; instead this is a region where considerable spatial as well as temporal variations prevail. For pulsatile flow, the WSS shows different behavior at different instants along the pipe. Oscillatory WSS is seen from the end of the stenosis to the exit. The immediate post-stenotic region is subject to a WSS in all directions, with the largest variation near peak systole, and during late diastole the WSS is either oriented straight forward or backward.

All components of the WSSG tensor were shown to be on the same order of magnitude, and thus neglecting the off diagonal terms might imply a severe underestimation.

Acknowledgements: The authors would like to thank Prof. S. H. Frankel, Purdue University, for providing the DNS data.

This work was supported by a grant from the Swedish research council, VR 2007-4085. Swedish National Infrastructure for Computing (SNIC) is acknowledged for computational resources provided by NSC, SNIC SNIC025/08-07.

References:

[1] A. M. Sallam and N. H. Hwang. Human red blood cell hemolysis in a turbulent shear flow: contribution of reynolds shear stresses. *Biorheology*, 1984.

[2] P. D. Stein and H. N. Sabbah. Measured turbulence and its effect on thrombus formation. *Circ. Res.*, 35:608–614, 1974.

[3] R. C. Becker, P. Eisenberg, and A. G. Turpie. Pathobiologic features and prevention of thrombotic complications associated with prosthetic heart valves: fundamental principles and the contribution of platelets and thrombin. *Am. Heart J.*, 2001.

[4] W. Nichols and M. O'Rurke. *McDonald's Blood Flow in Arteries*. Edward Arnold, 1990.

[5] A. M. Malek, S. L. Alper, and S. Izumo. Hemodynamic shear stress and its role in atherosclerosis. *Jama*, 282(21):2035–2042, 1999.

[6] C. Cheng, D. Tempel, R. van Haperen, A. van der Baan, F. Groseveld, and M. J. A. P. Daemen. Atherosclerotic lesion size and vulnerability are determined by patterns of fluid shear stress. *Circulation*, 2006.

[7] D. L. Fry. Acute vascular endothelial changes associated with increased blood velocity gradients. *Circ. Res.*, 22:165–197, Feb 1968.

[8] S. M. Schwartz, C. C. Haudenschild, and E. M. Eddy. Endothelial regneration. I. Quantitative analysis of initial stages of endothelial regeneration in rat aortic intima. *Lab. Invest.*, 38:568–580, May 1978.

[9] C.F. Jr. Dewey, S.R. Bussolari, M.A. Jr. Gimbrone, and P.F. Davies. The dynamic response of vascular endothelial cells to fluid shear stress. *J. Biomech. Eng.*, 1981.

[10] B. L. Langille, M. A. Reidy, and R. L. Kline. Injury and repair of endothelium at sites of flow disturbances near abdominal aortic coarctations in rabbits. *Arteriosclerosis*, 6:146–154, 1986.

[11] P.F. Davies, A. Remuzzi, E.J. Gordon, C.F. Jr. Dewey, and M.A. Jr. Gimbrone. Turbulent fluid shear stress induces vascular endothelial cell turnover *in vitro*. *Proc. Natl. Acad. Sci. USA*, 83:2114–2117, 1986.

[12] P. F. Davies. Overview: temporal and spatial relationships in shear stress-mediated endothelial signalling. *J. Vasc. Res.*, 34:208–211, 1997.

[13] P. F. Davies, K. A. Barbee, M. V. Volin, A. Robotewskyj, J. Chen, L. Joseph, M. L. Griem, M. N. Wernick, E. Jacobs, D. C. Polacek, N. dePaola, and A. I. Barakat. Spatial relationships in early signaling events of flow-mediated endothelial mechanotransduction. *Annu. Rev. Physiol.*, 59:527–549, 1997.

[14] K. A. Barbee, P. F. Davies, and R. Lal. Shear stress-induced reorganization of the surface topography of living endothelial cells imaged by atomic force microscopy. *Circ. Res.*, 74:163–171, Jan 1994.

[15] N. DePaola, M.A. Jr Gimbrone, P.F. Davies, and C.F. Jr. Dewey. Vascular endothelium responds to fluid shear stress gradients. *Arterioscler Thromb.*, 12(11):1254–7, Nov 1992.

[16] M.A. Haidekker, C.R. White, and J.A. Frangos. Analysis of temporal shear stress gradients during the onset phase of flow over a backward-facing step. *J Biomech Eng.*, 123(5):455–63, Oct 2001.

[17] G. A. Truskey, K. M. Barber, T. C. Robey, L. A. Olivier, and M. P. Combs. Characterization of a sudden expansion flow chamber to study the response of endothelium to flow recirculation. *J Biomech Eng*, 117:203–210, May 1995.

[18] C. R. White, M. Haidekker, X. Bao, and J. A. Frangos. Temporal gradients in shear, but not spatial gradients, stimulate endothelial cell proliferation. *Circulation*, 103:2508–2513, May 2001.

[19] C. Kleinstreuer, M. Lei, and J.P. Jr. Archie. Flow input waveform effects on the temporal and spatial wall shear stress gradients in a femoral graft-artery connector. *J Biomech Eng.*, 118(4):506–10, Nov 1996.

[20] M. D. Desphande and D. P. Giddens. Turbulence measurements in a constricted tube. *J. Fluid. Mech.*, 97:65–89, 1980.

[21] S. A. Ahmed and D. P. Giddens. Velocity measurements in steady flow through axisymmetric stenoses at moderate reynolds numbers. *J. Biomech.*, 16(7):505–516, 1983.

[22] S. A. Ahmed and D. P. Giddens. Flow disturbance measurements through a constricted tube at moderate reynolds numbers. *J. Biomech.*, 16(12):955–963, 1983.

[23] S. A. Ahmed and D. G. Giddens. Pulsatile poststenotic flow studies with laser doppler anemometry. *J. Biomech.*, 17(9):695–705, 1984.

[24] L. Antiga and D. A. Steinman. Rethinking turbulence in blood. *Biorheology*, 46:77–81, 2009.

[25] J. Ryval, A. G. Stratman, and D. A. Steinman. Two-equation turbulence modeling of pulsatile flow in a stenosed tube. *J. Biomech. Eng.*, 126:625–635, 2004.

[26] R. Mittal, S. P. Simmons, and F. Najjar. Numerical study of pulsatile flow ina constricted channel. *J. Fluid Mech.*, 485:337–378, 2003.

[27] R. Mittal, S. P. Simmons, and H. S. Udaykumar. Application of large-eddy simulation to the study of pulsatile flow in a modeled arterial stenosis. *J. Biomech. Eng.*, 123:325–332, 2001.

[28] S. E. Lee, S.-W. Lee, P. F. Fisher, H. S. Bassiouny, and F. Loth. Direct numerical simulation of transitional flow in a stenosed carotid bifurcation. *J. Biomechanics*, 41:2551–2561, 2008.

[29] S. S. Varghese, S. H. Frankel, and P. F. Fisher. Direct numerical simulation of stenotic flows. part 1. steady flow. *J. Fluid Mech.*, 582:253–280, 2007.

[30] S. S. Varghese, S. H. Frankel, and P. F. Fisher. Direct numerical simulation of stenotic flows. part 2. pulsatile flow. *J. Fluid Mech.*, 582:281–318, 2007.

[31] S. S. Varghese, S. H. Frankel, and P. F. Fisher. Modeling transition to turbulence in eccentric stenotic flow. *J. Biomech. Eng.*, 130:1–7, 2008.

[32] M. Germano, U. Piomelli, P. Moin, and W. H. Cabot. A dynamic subgrid-scale eddy viscosity model. *Phys. Fluids A*, 3(7):1760–1765, 1991.

[33] D. K. Lilly. A proposed modification of the germano subgrid-scale closure method. *Phys. Fluids A*, 4(3):633–635, 1991.

[34] S.-E. Kim. Large eddy simulation using unstructured meshes and dynamic subgrid-scale turbulence models. Technical report, AIAA Paper 2004-2548, 2004.

[35] *FLUENT 6.3 User's Guide*, September 2006.

[36] F. Mathey, D. Cokljat, J. P. Bertoglio, and E. Sergent. Specification of les inlet boundary condition using vortex method. In *4th International Symposium ln Turbulence, Heat and Mass Transfer*, Antalya, Turkey, 2003. Begell House, Inc.

[37] M. Lei, D.P. Giddens, S.cA. Jones, F. Loth, and H. Bassiouny. Pulsatile flow in an end-to-side vascular graft model: comparison of computations with experimental data. *J Biomech Eng.*, 123(1):80–7, Feb 2001.

[38] C. Kleinstreuer, J.R. Buchanan, M. Lei, and G.A. Truskey. *Computational Analysis of Particle Hemodynamics and Prediction of the Onset of Arterial Diseases, In: Cardiovascular Techniques: Biomechanical System*, volume II. CRC Press, Boca Raton, FL., 2001.

[39] J.R. Jr Buchanan, C. Kleinstreuer, G.A. Truskey, and M. Lei. Relation between non-uniform hemodynamics and sites of altered permeability and lesion growth at the rabbit aorto-celiac junction. *Atherosclerosis*, 143(1):27–40, Mar 1999.

[40] F.P. Glor, Q. Long, A.D. Hughes, A.D. Augst, B. Ariff, S.A. Thom, P.R. Verdonck, and X.Y. Xu. Reproducibility study of magnetic resonance image-based computational fluid dynamics prediction of carotid bifurcation flow. *Ann Biomed Eng*, 31(2):142–51, Feb 2003.

[41] M. Lei, C. Kleinstreuer, and G.A. Truskey. A focal stress gradient-dependent mass transfer mechanism for atherogenesis in branching arteries. *Med Eng Phys.*, 18(4):326–32, Jun 1996.

[42] L. Goubergrits, E. Wellnhofer, U. Kertzscher, K. Affeld, C. Petz, and H.C. Hege. Coronary artery WSS profiling using a geometry reconstruction based on biplane angiography. *Ann Biomed Eng*, 37(4):682–91, Apr 2009.

[43] J. Murphy and F. Boyle. Predicting neointimal hyperplasia in stented arteries using time-dependant computational fluid dynamics: a review. *Comput Biol Med.*, 40(4):408–18, Apr 2010.

[44] C. Kleinstreuer, S. Hyun, J. R. Buchanan, P. W. Longest, J. P. Archie, and G. A. Truskey. Hemodynamic parameters and early intimal thickening in branching blood vessels. *Crit Rev Biomed Eng*, 29:1–64, 2001.

[45] S.M. Kute and D.A. Vorp. The effect of proximal artery flow on the hemodynamics at the distal anastomosis of a vascular bypass graft: computational study. *J Biomech Eng.*, 123(3):277–83, Jun 2001.

[46] M. Ojha. Spatial and temporal variations of wall shear stress within an end-to-side arterial anastomosis model. *J Biomech*, 26:1377–1388, Dec 1993.

[47] J. F. LaDisa, L. E. Olson, H. A. Douglas, D. C. Warltier, J. R. Kersten, and P. S. Pagel. Alterations in regional vascular geometry produced by theoretical stent implantation influence distributions of wall shear stress: analysis of a curved coronary artery using 3D computational fluid dynamics modeling. *Biomed Eng Online*, 5:40, 2006.

[48] S. J. Sherwin and H. M. Blackburn. Three-dimensional instabilities and transition of steady and pulsatile axisymmetric stenotic flows. *J. Fluid Mech.*, 533:297–327, 2005.

[49] F. G. Ghalichi, X. Deng, A. De Champlain, Y. Douville, M. King, and R. Guidoin. Low reynolds number turbulence modeling of blood flow in arterial stenoses. *Biorheology*, 35(4,5):281–294, 1998.

[50] M. Zijlema, A. Segal, and P. Wesselinh. Finite volume computation lf 2d incompressible flows in general coordinates in staggerd grids. *Int. J. Numer. Methods in Fluids*, 20:621–640, 1995.

[51] J. Lantz, J. Renner, and M. Karlsson. Wall shear stress in a subject specific human aorta - influence of fluid-structure interaction. *Int. J. Appl. Mech.*, In press, 2011.